Research on the Dynamic Response of High-speed Trains under Different Curve Radii Caused by Wind–sand Flow

Y. Bai, Z. N. Zhang[†], Z. F. Wang, T. M. Li and Y. J. Wang

School of Civil Engineering, Beijing Jiaotong University, Beijing, 100044, China

†*Corresponding Author Email: 21121219@bjtu.edu.cn*

ABSTRACT

To investigate how the curve radius parameter affects the safety of high-speed train operation in a wind–sand environment, researchers used the wind–sand section of the Lanzhou–Urumqi high-speed railway as their research backdrop. The Euler–Lagrange method was used to discretize the sand particles based on train aerodynamics theory, and the wind–sand flow model of the head–middle–tail three-member formation was established. The accuracy of the model was verified by comparing the data from published papers, and then the train's wind–sand load was calculated and extracted. Subsequently, a dynamic model of a CRH2 train was created, and the dynamic response of the train was estimated by choosing various curve radii and adding wind–sand loads. The results demonstrated that as wind speed increases, the forces acting on the train due to wind rise. Due to the different shapes and positions of the carriages, the wind–sand load on each car differs; the middle car is subjected to greater lift, lateral force, and overturning moment, as well as lower resistance, nodding moment, and head shaking moment, while the head and tail cars move in the opposite direction and, as a whole, are exposed more adverse forces. The study found that when the curve radius increased from 7000 to 9000 m, the derailment coefficient and wheel-rail lateral force are reduced by approximately 29%~32%, along with an approximately 20%~23% decrease in the wheel load reduction rate. When the radius reaches 10000 m, there is a decrease in the derailment coefficient and wheel-rail lateral force of approximately 5%~8%, as well as a reduction in the wheel weight load reduction rate of approximately 3%~6%. It has been concluded that increasing the curve radius can significantly reduce the safety indices in the wind-blown sand environment, thus improving operational safety. However, it should be noted that a radius of 8000~9000 m is appropriate, and the effect of further increase is not obvious. The results of this study can provide certain guidance for the selection of curve radius and the evaluation of the operational safety of high-speed trains in windy–sandy areas.

1. INTRODUCTION

The construction and safe operation of railways in sandy areas have been plagued by wind and sand disasters. China ranks first in the world in terms of railroad mileage in sandy areas, with a cumulative length of approximately 1.5×10^4 km (Zhang et al., 2019b), which is mainly concentrated in the northwestern region. Strong wind conditions are complex external conditions that affect the safety of railway operation (Bergstrom et al., 1992; Feng & Lu 1994; Cheng & Xue, 2014); additionally, these meteorological conditions develop in the northwest every spring and autumn due to the influence of crosswinds from

the wind gap, and the structural characteristics of wind–sand flow in this region are completely different from those in ordinary desert areas. The wind–sand flow formed under the influence of strong winds creates sand impact pressure (Jiang et al., 2010), which repeatedly results in broken tempered glass windows, buried tracks, and destroyed railway equipment, resulting in train derailments, stoppages, casualties and economic losses (Gao et al., 2018). Therefore, operational safety training under strong wind–sand flow conditions is a topic worth studying.

Many researchers have undertaken numerous studies in the past to increase the stability of high-speed trains in

NOMENCLATURE

LES	Large Eddy Simulation		*DPM*	Discrete Phase Model
UDF	User Defined Functions		*CFD*	Computational Fluid Dynamics
UIC	International Union of Railways		*CRH*	China Railways High-speed
DES	Detached Eddy Simulation		u_z	wind speed at height z
u^*	frictional or shear velocity		k	Karman constant
z	height		τ	surface shear stress
ρ	air density		σ_p	particle density-to-air density ratio
g	gravitational acceleration		d_p	sand grain diameter
ρ_p	sand density		Γ	diffusivity
G	turbulence production term		Y	turbulence dissipation term
D_ω	cross-diffusion term		u_{pi}	sand velocity component
u_i	air velocity component		t	time
μ	dynamic viscosity		C_{Dp}	drag coefficient
Re_p	relative Reynolds number		g_i	gravitational acceleration component
C_{Fs}	lateral force coefficient		A	reference area
u	synthetic wind speed		C_{Fl}	lift force coefficient
C_{Mr}	overturning moment		h	height of the car section
M	mass matrices		C	damping matrices
K	stiffness matrices		X	generalized displacement vector
$\dot{X}$	generalized velocity vector		$\ddot{X}$	generalized acceleration vector
F	generalized load vector			

crosswind situations, concentrating mostly on shape design, wind conditions, substructures, and windbreak fences, among other factors. Using wind tunnel experiments and numerical simulations, Suzuki et al. (2003), Chang et al. (2021), and Adamu et al. (2022) discovered that the form of the train and dimension length impact the aerodynamic properties of the train. Khier et al. (2000) used the finite volume discrete method to obtain the flow field around a train under different wind conditions and Reynolds numbers; their results showed that the wind angle has a significant effect on the vortex, and they also studied the pressure distribution on the surface of a high-speed train and the laws of aerodynamic resistance and the coefficient of the side-rolling moment varying with the wind angle. Baker et al. (2009), Wang et al. (2018), and Noguchi et al. (2019) investigated the aerodynamic characteristics of high-speed trains on embankments and bridges in a crosswind environment and discovered that the aerodynamic forces of trains are related to the shape of the bridge and embankment foundations and increase with the thickness of the bridge and roadbed. Wind tunnel experiments were used to verify and assess the results. Zhang et al. (2017a) and Zhang et al. (2019a) evaluated the effect of adjusting the shape of the windbreak fence on train speed. Hemida et al. (2005), Krajnovic et al. (2012), and Zhang et al. (2017b) used the LES method to simulate a high-speed train under crosswind conditions and found that the flow field and aerodynamic forces predicted by LES agree well with the experimental data. Furthermore, researchers have investigated travel safety from the standpoint of vehicle dynamics. Li et al. (2010) proposed a Fluent and Simpack-based fluid–structure coupling cosimulation method for high-speed trains by comparing the differences in train aerodynamic force and attitude, safety, and comfort indices between the two methods of joint simulation and offline simulation and verified the differences in train aerodynamic force and attitude, safety, and comfort indices when joint simulation and offline simulation are

considered. The importance of evaluating the fluid–structure coupling impact was established in this investigation. You et al. (2018) utilized Simpack to model a vehicle's dynamic properties and safety when it is running on a curve during a gust of wind. When the wind speed exceeded 25 m/s, the derailment coefficient of the wheels on the outside track considerably exceeded the safety threshold, resulting in derailment and overturning.

A series of research results on the role of wind and sand impact forces on high-speed trains in wind–sand environments are also available. Paz et al. (2015) and others studied the influence of sand impact on train operation using Fluent's DPM model and discovered that, in the case of a small side collision angle and high speed, the head car of a train is subject to a greater probability of impact, and the impact effect of the sand particles on the train increases with the diameter of the sand particles; for every reduction in the collision recovery coefficient of the sand particles, the sand grain force on the train decreases by 10%. Wang et al. (2019) investigated the effects of sand particle characteristics (particle diameter and recovery coefficient) on the aerodynamic performance of a head car as well as the effect of the yaw angle of sandy flow on the aerodynamic coefficient; their results showed that a larger yaw angle contributes to the aerodynamic force of the head car and the effect of sand particle characteristics on the aerodynamic coefficient. Xiong et al. (2011) performed numerical simulations of the aerodynamic characteristics of trains operating at various sandstorm levels, derived train stability equations from a dynamic standpoint using moment balance theory, and calculated recommended speed limits for trains operating at various sandstorm levels. To analyze the operational safety of high-speed trains under sandstorm conditions, Li et al. (2012b) suggested a semicoupled solution method based on vehicle–track coupled dynamics and aerodynamics. Du et al. (2020) used Fluent to investigate the effect of broken windows on the aerodynamic performance of a train model in a strong wind–sand environment, and the

absolute values of the side force and overturning moment increased significantly as the number of broken windows on the windward side increased. With an increase in the number of damaged windows on the windward side, the absolute values of the side force and overturning moment increased dramatically.

The issue of intense sand flow in desert regions has emerged as a significant concern, causing several challenges for railway operations in China and the Middle East (Bruno et al., 2018), including countries such as Saudi Arabia and Iran. Numerous factors affect high-speed train operations in wind-blown sand conditions. In contrast to other regions, the sand and gravel carried by strong winds have a more significant impact. The combined impact of wind-blown sand can erode train bodies (Woldman et al., 2012; Paz et al., 2015), break windows (Du et al., 2020; Deng et al., 2021b), affect passenger comfort (Montenegro et al., 2022; Srivastava et al., 2022), bury compressed tracks, damage railway facilities along lines, and even lead to risks such as derailment and overturning of trains (Zhang et al., 2015; Liu et al., 2020; Deng et al., 2021a). Tremendous loss of life and property has occurred. Previous studies on the driving safety of high-speed trains under windy and sandy conditions have focused primarily on factors such as the wind speed, wind direction, sand properties, and structural integrity of the tracks. In addition, high-speed trains that travel on curved tracks are susceptible to the influence of crosswinds and curved rails on each side (Andersson et al., 1996; Liu et al., 2019). In the curved section, the force and direction of lateral wind and sand on the train are constantly changing (Wang et al., 2019), causing the train to lean to one side, which greatly increases the derailment coefficient and rate of wheel weight of the train, which poses great risks to the safe operation of the train.

However, there is currently a lack of research on the influence of curve radius parameters on train safety operations in sandstorm areas. Therefore, this paper adopts a method that combines fluid simulation and vehicle-rail dynamic response to study the influence of the curve radius on train safety under the action of sandstorm flow. This approach fully considers the influence mechanism of sandstorms on trains in the initial design stage, optimizes curve design parameters, and ensures the safety of railway operation. This study provides design parameters for the curved section of high-speed railways in sandy areas.

2. REGIONAL WIND-SAND CONDITIONS

2.1 Wind Speed and Direction

In this paper, the Lanzhou–Urumqi high-speed railway is the main research object; it passes through five major wind zones along its route (Meng et al., 2018), which have long wind durations, high wind speeds and stable directions. Among them, the Baili Wind Zone is the most typical wind zone (see Fig. 1) with the strongest wind and the longest length (Xiao et al., 2016), and it is used as the research object because of the abundant measurement data in this zone.
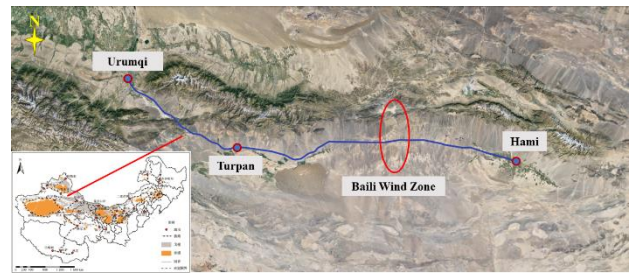

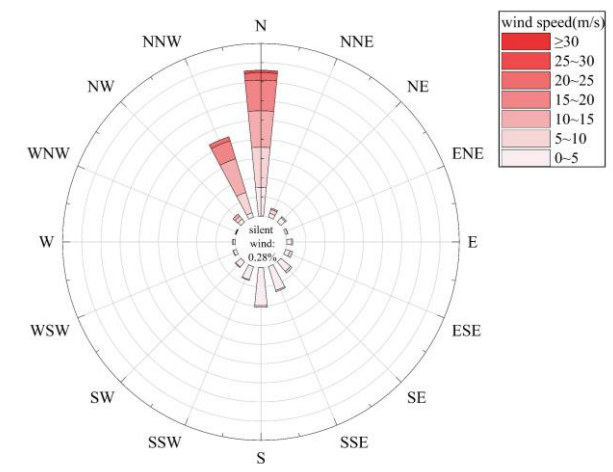**Fig. 1 Schematic of the Lanzhou–Urumqi Railway**

Fig. 2 Diagram of the wind power data

The daily wind data from 2020–2023 were obtained from the National Centers for Environmental Information (NCEI) (see Fig. 2). The prevailing wind direction in the Shisanjianfang Area, located in the center of the Baili Wind Area, is mainly concentrated in the N and NNW directions, accounting for 38.3% and 21.9% of the year, respectively, and the strongest wind season is from April to June; the measured average wind speed is approximately 8.15 m/s throughout the year, and the annual average number of windy days is 134 days, of which more than 25 m/s of windy days average 42 days, accounting for 11.5%.

The Lanzhou–Urumqi high-speed railway in the Baili Wind Zone in the line direction is basically perpendicular to the prevailing wind direction; the wind speed acts on the train for the full wind speed, and the danger of the train being blown over by strong crosswinds is greatly increased. According to the observational data of the Xinjiang Meteorological Service Center (Jiang et al., 2020), the safe warning wind speeds during train operation in the Baili Wind Zone are shown in Table 1.

Table 1 Safety warning wind speeds train operation

Ambient Wind Speed,m/s	Operating standards
$20 \leq w < 25$	200 km/h
$25 \leq w < 30$	160 km/h
$30 \leq w < 35$	80 km/h
$w \geq 35$	Out of service

2.2 Wind Speed Profile

The wind speed profile is a distribution curve used to describe the degree to which the wind speed varies with altitude. The figure shows that different distributions are influenced by atmospheric stability and have different distribution patterns in the vertical direction. Using the typical wind speed profile theory (Bruno et al., 2018), the relationship between the wind speed and height is given by

$$u_z = \frac{u^*}{k} \cdot \ln \frac{z}{z_0} \tag{1}$$

$$u^* = \left(\tau/\rho \right)^{\frac{1}{2}} \tag{2}$$

where u_z is the wind speed at height z; u^* is the frictional or shear velocity; τ is the surface shear stress; ρ is the air density; k is the Karman constant, which generally takes the value 0.4; and z_0 is the surface roughness.

The linear correlation between the logarithm of the wind speed and the height is easily known, and the correctness of this law is also shown by the measured data of the vertical wind gradient near the ground in the 100-mile wind range (Sun & Zhang, 2019). The same is true for the velocity of sand grains as well as for von Karman's law of logarithmic velocity distribution.

2.3 Particle Size and Threshold Friction Velocity

The vertical distribution curve of sand accumulation directly reflects the structural features of wind–sand flow, and this curve is critical for understanding the movement characteristics of wind–sand flow. Because the diameter of the sand grains in the model varies, particle analysis may help to better understand the structure of wind–sand flow as well as the law of wind–sand flow movement.

The data obtained from this railway wind–sand environment study indicate that the sand particles at a height of 0~10 m are predominantly found within the size range of 0.1 mm to 0.25 mm. Approximately 20% of the total sand particles have sizes ranging from 0.25 mm to 0.5 mm and from 0.075 mm to 0.1 mm. Only 2% of the sand particles had sizes larger than 2 mm (Jiang et al., 2010).

Because the momentum required for the movement of sand grains in nature is provided by air movement and because the movement of sand particles with a larger particle size or higher density has difficulty occurring, the starting wind speed is critical for studying the generation and strength of wind–sand flow. The critical friction velocity hypothesis (Sharratt & Vaddella, 2014) states that

$$u_{*t} = \sqrt{A_N \left(\sigma_p g d + \frac{\gamma}{\rho_p d_p} \right)} \tag{3}$$

where A_N and γ are constants of 0.0123 and 3×10^{-4} $kg\ s^{-2}$, respectively; σ_p is the particle density-to-air density ratio; g is the gravitational acceleration, m/s^2; d_p is the sand grain diameter, m; and ρ_p is the sand grain density, kg/m^3.

According to the Lanzhou Desert Institute of the Chinese Academy of Sciences field observations of wind

Table 2 Threshold friction velocity

Particle size, mm	Speed, m/s	
	H=6 m	H=8 m
1~1.25	15.2	16.0
1.25~2.5	20.1	21.1
2.5~5	26.5	27.8
5~10	35.0	36.7
10~20	46.2	50.5
20~40	61.0	64.0
40~80	80.5	84.5

speed data of different grain sizes in the wind area along the Lanzhou–Xinjiang route (as shown in Table 2), wind speeds greater than 8 can cause surface sand grains to move (Wu et al., 2010).

2.4 Wind–Sand Flow Density

Wind speed and height fluctuations complicate the distribution of sand particle sizes in wind–sand flow, making it difficult to investigate the spatial distribution pattern of sand grains in each grain size group. To avoid discussing the complexities of particle size composition, researchers have focused on the mechanical properties of sand material as a whole and thus used the density of wind–sand flow (Niu et al., 2020), which is the mass of sand material per unit volume of wind–sand flow at different heights, to represent the structural characteristics of wind–sand flow.

In this paper, we use the wind and sand data from the Shisanjianfang Area under conditions similar to those used in Jiang Fuqiang's (Jiang et al., 2010; Li et al., 2010) study to simulate the structural characteristics of extreme wind–sand flows encountered during the operation of the Lanzhou–Xinjiang high-speed railway. In the literature, observed wind–sand flow density data within 9 *m* of the ground under various wind speed circumstances in the Shisanjianfang Area are reported. The wind–sand flow density was compared to the height data curves and fitted to the observed data to compute the sand content in each height range at the different wind speeds.

$\rho = A \times exp(B \times z) + C$ is chosen as the fitting equation for the computation in this study, and the fitting equation of the wind–sand flow density compared to the height at different wind speeds is as follows:

$$\rho_{v=20} = 1.691 \times 10^{-4} \times e^{-0.223z} - 2.654 \times 10^{-6} \quad (R^2 = 0.95326)$$

$$\rho_{v=25} = 5.863 \times 10^{-4} \times e^{-0.518z} + 5.734 \times 10^{-5} \quad (R^2 = 0.97825)$$

$$\rho_{v=30} = 1.942 \times 10^{-2} \times e^{-0.814z} - 3.156 \times 10^{-5} \quad (R^2 = 0.98751)$$

The fitted curves of the wind–sand flow density versus height for different wind speeds are shown in Fig. 3.

3. COMPUTATIONAL MODELS

3.1 Basic Theoretical Equations

To investigate the impact of wind and sand flow on train aerodynamics, it is vital to analyze not only the influence of high winds on trains but also the combined impact of high winds and blown-up sand particles on high-
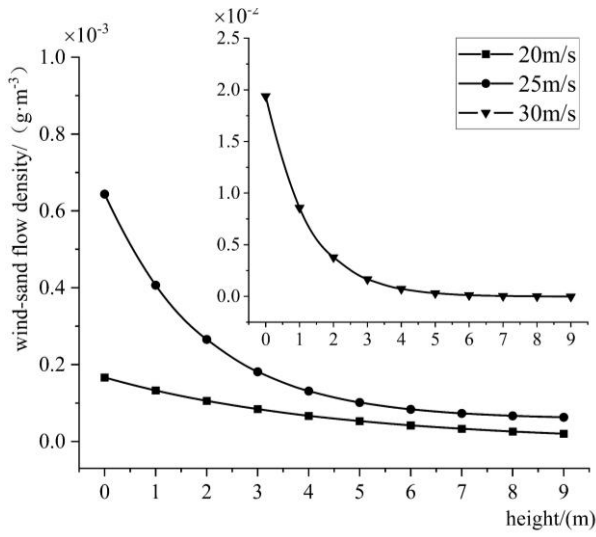
Fig. 3 Wind–sand flow density against height fitting curve

speed trains. Wind–sand flow is a typical two-phase air–solid flow, and its numerical simulation comprises both continuous-phase air and discrete-phase sand particles. Due to the low concentration of sand in the air, which is much less than 10% (Zhang et al., 2023), this article employs the DPM model to simulate a sandy environment. The Navier–Stokes equation is used to solve the flow field around the train for the Euler fluid part. The turbulence model is used in the SST model, which is widely used in the aerodynamic calculation of high-speed trains (Yu et al., 2021), and its expression is:

$$\rho \frac{\partial(k\bar{u}_i)}{\partial x_i} = \frac{\partial}{\partial x_j}(\Gamma_k \frac{\partial k}{\partial x_j}) + G_k - Y_k \tag{4}$$

$$\rho \frac{\partial(\omega\bar{u}_i)}{\partial x_i} = \frac{\partial}{\partial x_j}(\Gamma_\omega \frac{\partial \omega}{\partial x_j}) + G_\omega - Y_\omega + D_\omega \tag{5}$$

where Γ is the diffusivity, G is the turbulence production term, Y is the turbulence dissipation term, and D_ω is the cross-diffusion term.

The Lagrange equation of motion is used for the discrete-phase sand fraction (Wu et al., 2015):

$$\frac{du_{pi}}{dt} = \frac{18\mu}{\rho_p d_p^2} \frac{C_{Dp} \operatorname{Re}_p}{24}(u_i - u_{pi}) + \frac{g_i(\rho_p - \rho)}{\rho_p} \tag{6}$$

where u_{pi} is the sand velocity component, u_i is the air velocity component, t is time, μ is the dynamic viscosity, ρ_p is the sand density, ρ is the air density, d_p is the sand particle size, C_{Dp} is the drag coefficient, Re_p is the relative

Reynolds number, and g_i is the gravitational acceleration component.

Here, the relative Reynolds number is defined as follows:

$$\operatorname{Re}_p = \frac{\rho d_p |u_p - u|}{\mu} \tag{7}$$

The primary aerodynamic performance metrics of high-speed trains in windy and sandy settings include the aerodynamic lateral force coefficient (Liu et al., 2011), aerodynamic lift force coefficient, and aerodynamic overturning moment coefficient. This provision contains the following expressions:

$$C_{F_s} = \frac{F_s}{0.5\rho A u^2} \tag{8}$$

$$C_{F_l} = \frac{F_l}{0.5\rho A u^2} \tag{9}$$

$$C_{M_r} = \frac{M_r}{0.5\rho A h u^2} \tag{10}$$

where C_{Fs} is the lateral force coefficient, A is the reference area, u is the synthetic wind speed, C_{Fl} is the lift force coefficient, C_{Mr} is the overturning moment, and h is the height of the car section.

3.2 Wind-Sand Flow Model

The CRH2-type rolling stock operates on the Lanzhou–Xinjiang High-Speed Railway at a speed of 250 km/h. This study uses a Rhino 6 train geometry model utilizing this car as the prototype. Because the rolling stock structure is quite complicated, a simulation that is too precise demands high computer performance and has little influence on the accuracy of the findings; thus, the training model is simplified.

This high-speed train's simplified model (Fig. 4) is a three-section formation of the head car, middle car, and tail car, with a width of 3.3 meters, a height of 3.86 meters, a length of 24.5 meters for the middle car, and a length of 25.7 meters for the head and tail cars, with the same external dimensions.

To decrease the computational volume while satisfying the calculation accuracy, the calculation domain should be as compact as possible. The simulation can obtain more realistic results when the blockage rate of the bypassed item in the computational domain is less than 5% and the position is suitably selected (Li, 2012). The calculation area is 300 m in length, 100 m in width, and 40
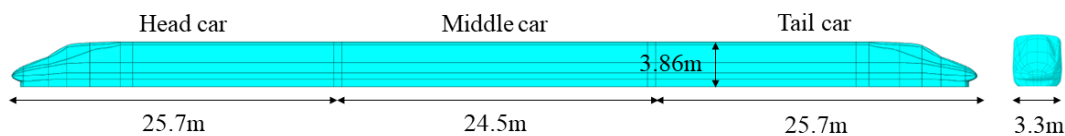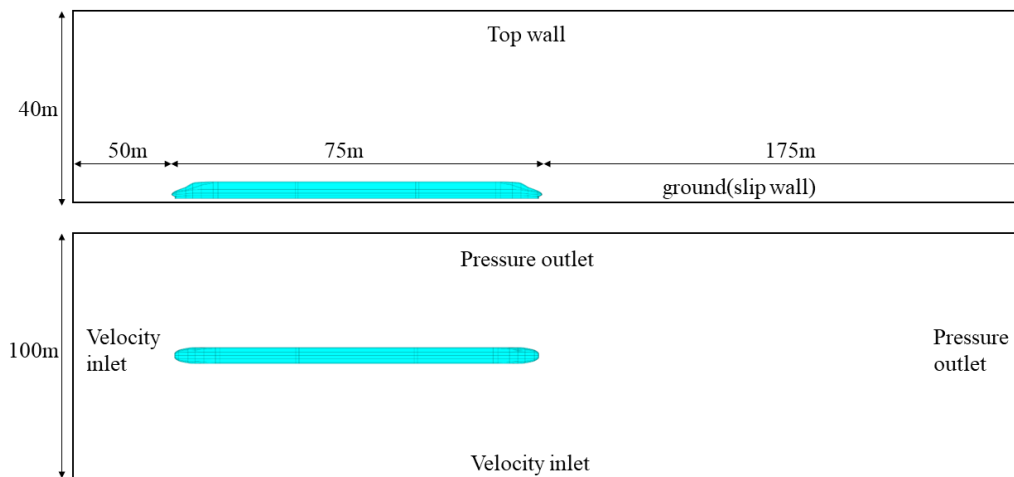

Fig. 4 Geometry model

Fig. 5 Computational domain

Table 3 Boundary conditions

Boundary	Continuous-phase (air)	Discrete-phase (sand particles)
Front	Velocity inlet	escape
Back	Pressure outlet	escape
Left	Velocity inlet	escape
Right	Pressure outlet	escape
Top	Symmetry	——
Bottom	wall	trap
Train	wall	reflect

m in height to allow the wind and sand to fully operate on the train, guarantee that the fluid conditions are fully developed, and prevent backflow from creating false calculation results. A 0.376 m space is left between the train model and the ground to replicate the gap between the lowermost section of the train sidewall and the ground. Figure 5 and Table 3 provide details for the computational domain and boundary conditions.

The computational domain entrance is designated the velocity entrance, the exit is designated the free pressure exit, the train surface is designated the no-slip wall boundary, the ground is designated the relative slip wall boundary, and the slip velocity is equal to the train velocity in the opposite direction to simulate the ground effect. A function in the C programming language that incorporates the gas phase, sand phase velocity, and sand phase concentration (as indicated by the fitting formula depicted in Fig. 3) is created in the model using a user-defined function (UDF). The sand particle size should fall within the range of 0.1 mm to 0.25 mm, and the average distribution should be utilized as input. The model uses steady-state computations.

This model uses Fluent 2021R1 to generate a mesh utilizing polyhexore meshes. Upon completion of the meshing process, the total number of meshes is 8 million. Figure 6 displays the flow field, train body, and boundary layer meshes. This model primarily examines the aerodynamic force exerted on trains at varying wind speeds. Studying the impact of the boundary layer on a train surface is crucial. The train body is equipped with six
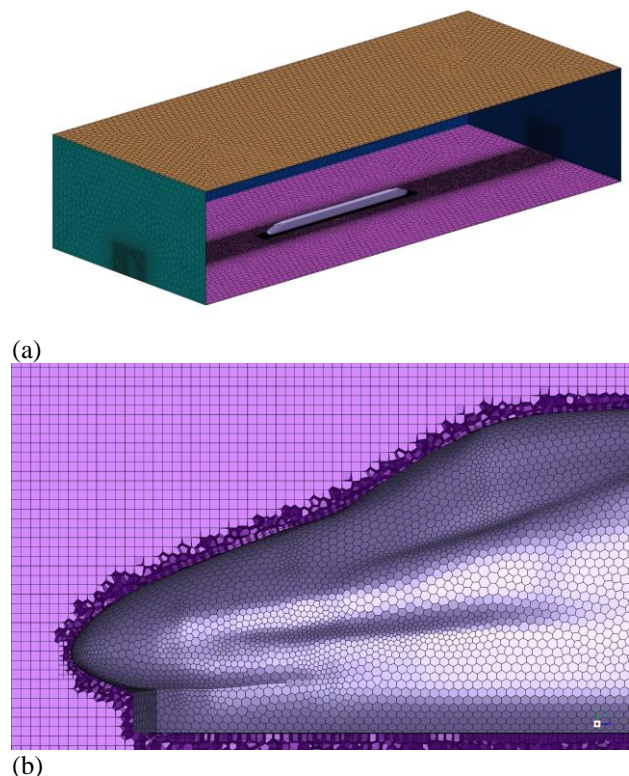

(a)

(b)

Fig. 6 Computational mesh

(a) Global mesh (b) Train body and boundary layer mesh
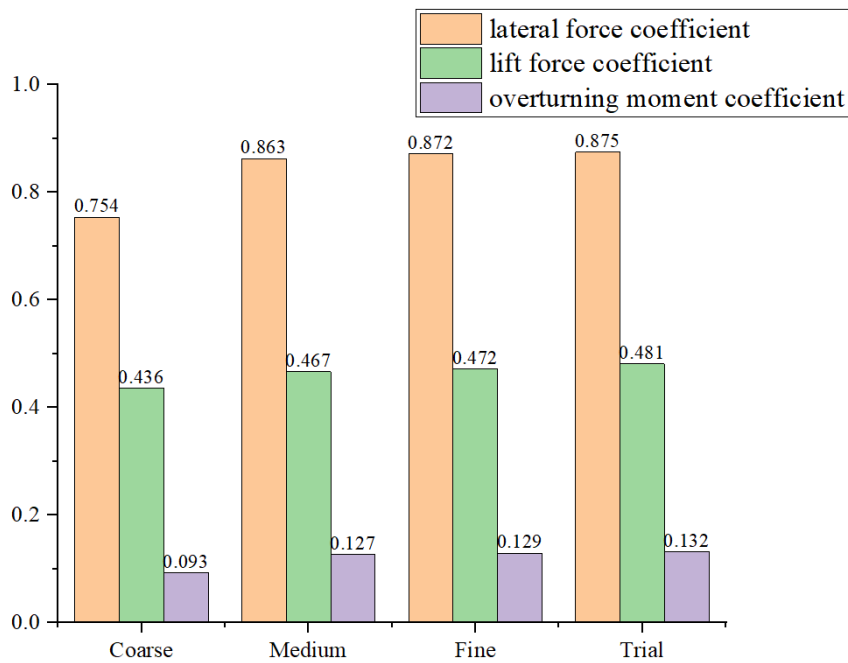
Fig. 7 Mesh independence

layers of boundary layer grids near its surface. The rate of grid expansion is 1.2. The first layer has a thickness of 0.01 mm to ensure that the y+ of the train surface closely approximates 1, as per the specifications of the SST *k-ω* turbulence model. When partitioning the grid, it is imperative to perform local refinement of the grid near the train and separate the remote computation region into sparser grids. Implementing this measure can enhance the grid's quality and decrease the time it takes for the model computation to converge.

In the solution process, a pressure-based solver is used for simulation, and a second-order upwind scheme is used to solve the momentum equation, k equation, and ω equation. The calculation method adopts the SIMPLEC algorithm to realize the coupling of the pressure field and velocity field. The aerodynamic load of the car body is monitored until the change in force becomes stable with each iteration.

3.3 Validation of the Models

The quantity and quality of meshes exert a substantial influence on the precision of the computational outcomes, necessitating the confirmation of mesh independence. To start the validation process, the disparities across the different grids (namely, coarse, medium, and fine) are assessed by considering identical y+ values. Therefore, it is guaranteed that the highest values of grid skewness are all less than 0.8, as is the case for the identical solution method. This research focuses on the lateral force coefficients, lift force coefficients, and overturning moment coefficients as the criteria. Figure 7 presents a comparison between the estimated aerodynamic coefficients of high-speed trains (with a wind speed=25 m/s) and the proven trial results (Xi, 2012; Zhang et al., 2017b) using various size grids. Fig. 7 illustrates that the disparity between the computed coefficients of the fine

and medium grid models and the established trial values is minimal, with an error margin of less than 5%. This level of precision satisfies the demands of engineering calculations. Simultaneously, the computation outcomes for the fine grid and medium grid exhibit minimal disparity, with a variation of less than 2%. Therefore, by accounting for computational efficiency, this study opts for a medium grid to conduct high-speed train aerodynamic calculations. It is firmly believed that the developed wind–sand flow train model exhibits robust reliability.

3.4 Model of train system dynamics

The dynamics of train systems are primarily concerned with vehicle dynamics and wheel–track connections. The train system dynamics equation is solved using the assumption that the train body, frame, and wheel pair are rigid bodies with no elastic deformation. The train system dynamics equation is

$$M\ddot{X} + C\dot{X} + KX = F \qquad (11)$$

where *M*, *C* and *K* are the train system's mass, damping, and stiffness matrices, respectively; *X* is the system's generalized displacement vector; $\dot{X}$ is the system's generalized velocity vector; $\ddot{X}$ is the system's generalized acceleration vector; and *F* is the system's generalized load vector, which includes the track excitation load and the aerodynamic load acting on the center of mass.

Simpack software is used to construct a high-speed railway train system dynamics model. The vehicle dynamics model and the wheel–track interaction are the two fundamental components of the railway train system dynamics model. The train dynamics model contains the train body, bogie, and wheel pair, and so on, with each component considered a rigid body without regard for elastic deformation. The train body, bogie, and wheel pair
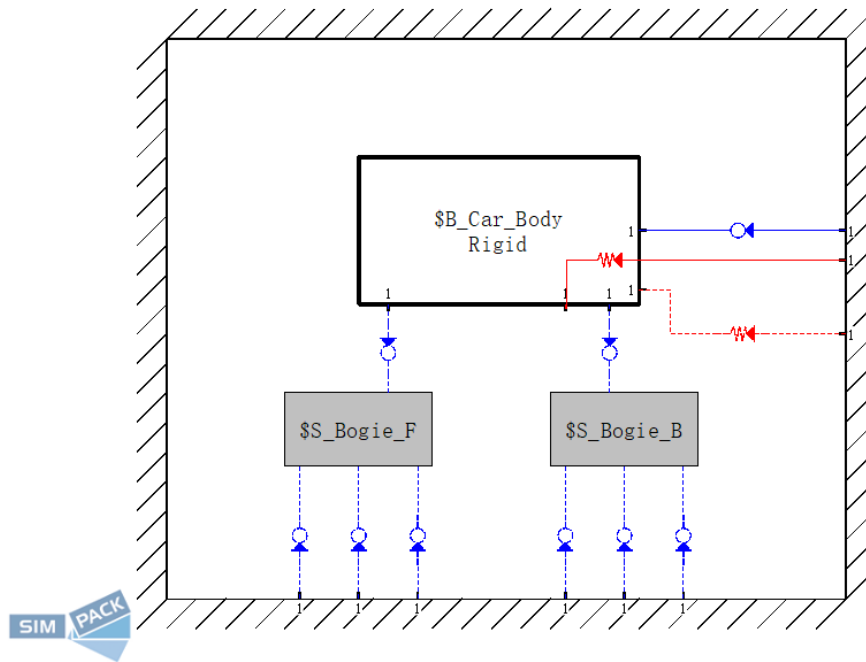
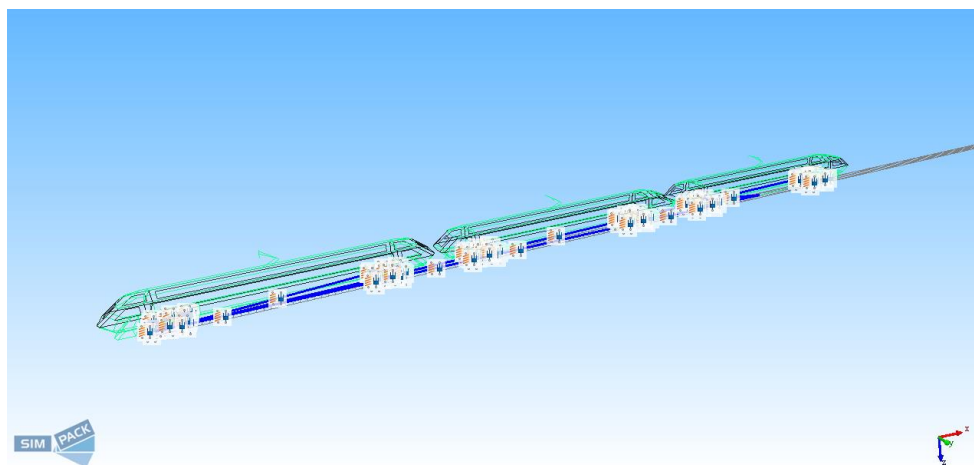**Fig. 8 Topology of the train body**

Fig. 9 The complete training model

have 6 degrees of freedom, as do the rocking head, nodding head, traverse, telescoping, side-rolling, and transverse pendulum, and the entire car system may be condensed to a 42-degree-of-freedom multirigid body model. Between the wheel pair and the bogie, the primary suspension system is utilized, and between the train body and the bogie, the secondary suspension system is employed. Since the structures of the front and rear bogies are exactly the same, the bogies are used as the substructure. When creating the secondary suspension, the virtual car body is introduced so that the primary suspension and the second row suspension are well performed in the bogie model, avoiding the repeated creation of the secondary suspension in the main model. At the same time, in the bogie model, the parameters of the front and rear wheelsets are exactly the same, so the wheelset model is treated as the substructure of the bogie model.

The wheel tread in this study is an S1002 wear-type tread, the rail is a GB 60 rail, and the wheel–rail contact force is estimated using Hertz contact theory and the Kalker-FASTSIM method. The track spectrum for the Lanzhou–Xinjiang high-speed railway is a German low-interference track spectrum because the design speed is 250 km/h.

Joint 7 is used to represent the movement of the car body, wheels, and frame with respect to the ground, and to better represent the actual force condition of the train, the hysteresis force element 104 is used in Simpack to replicate the operation of the hook buffer to construct a multitrain body model. Because the train body is rigid, its shape has little to no effect on the model simulation results; therefore, the same shape is used for all three car bodies. Figures 8 and 9 show the single train body topology and the complete car model.

(a)

(b)
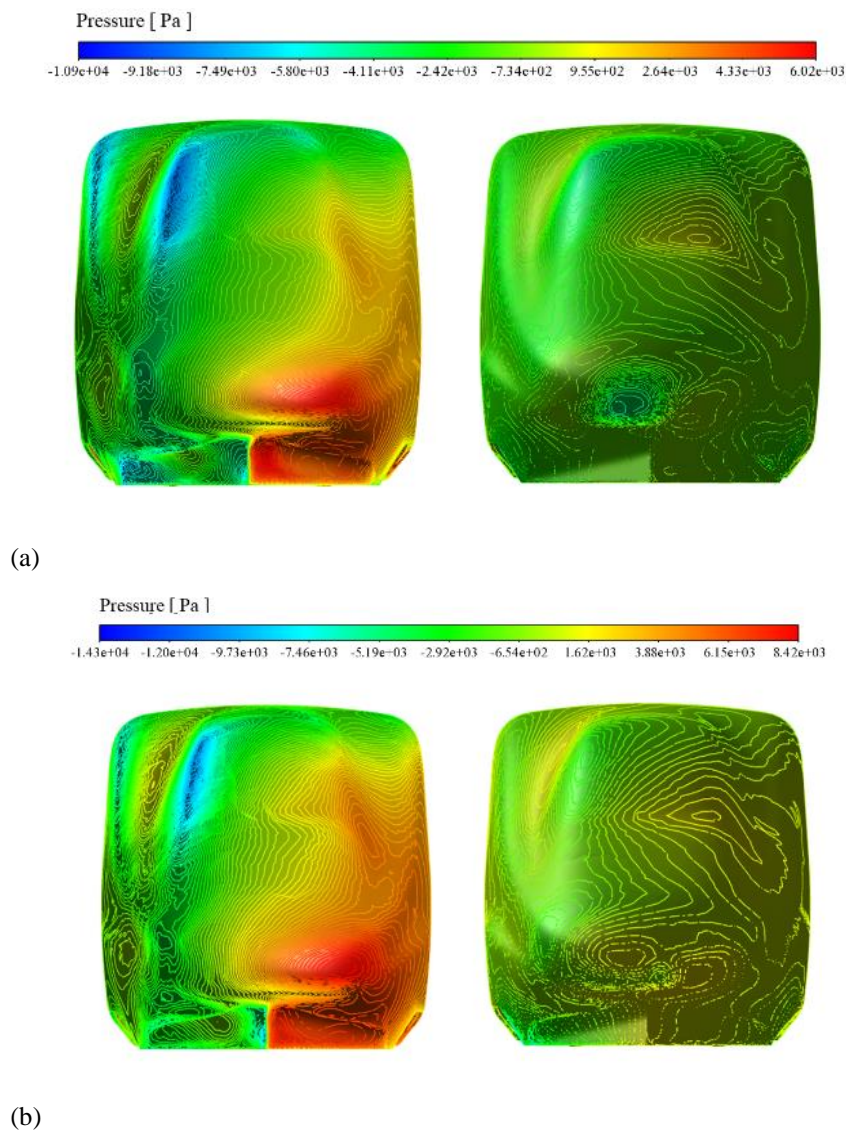
Fig. 10 Head and tail pressure field

(a) without sand and (b) with sand

4. FACTOR ANALYSIS

The pressure distributions of the head car, tail car, and body without sand and under sand conditions at a wind speed of 25 m/s and train speed of 250 km/h are illustrated in Figs. 10–11. Under crosswind conditions, synthetic wind blows toward trains due to the superposition of high-speed running wind with trains. As depicted in Fig. 10(a) and 11(a), under conditions without sand, the primary impact point of the synthetic wind is on the nose cone of the head car. Due to air viscosity, the synthetic wind ceases when it reaches the nose cone, resulting in almost zero wind speed and the highest pressure. The maximum positive pressure is 6.02×10^3 Pa, while above the leeward side of the nose, the maximum negative pressure occurs. At the tail section, pressures decrease due to accelerated airflow, resulting mostly in negative surface pressures on the tail car; positive pressures are experienced on the windward side of the body, whereas negative pressures prevail on the leeward side.

The pressure distribution trend of the vehicle body under sand conditions can be observed in Fig. 11(a) and 11(b), which remain consistent. The windward side of the front car exhibits a larger area of positive pressure, with the maximum positive pressure increasing from the initial value of 6.02×10^3 Pa to 8.41×10^3 Pa, indicating a growth rate of 39.6%. As a result of the sand particles carried by the synthetic wind, there is continuous enhancement in the coupling force between the wind and sand on the head car, leading to further reduction in negative high-pressure areas on its leeward side. Consequently, the maximum negative pressure decreases from 1.09×10^3 Pa to 1.43×10^3 Pa. Moreover, due to sand particle impact, there is reduced negative pressure on the front surface of the tail car, while an increased area of positive pressure becomes evident.

Figure 12(a)-(f) shows the relationships between the train aerodynamic loads and the wind speed, and the trends are basically the same: the aerodynamic force of each car increases with increasing wind speed, and the higher the wind speed is, the more significant the changes in the force
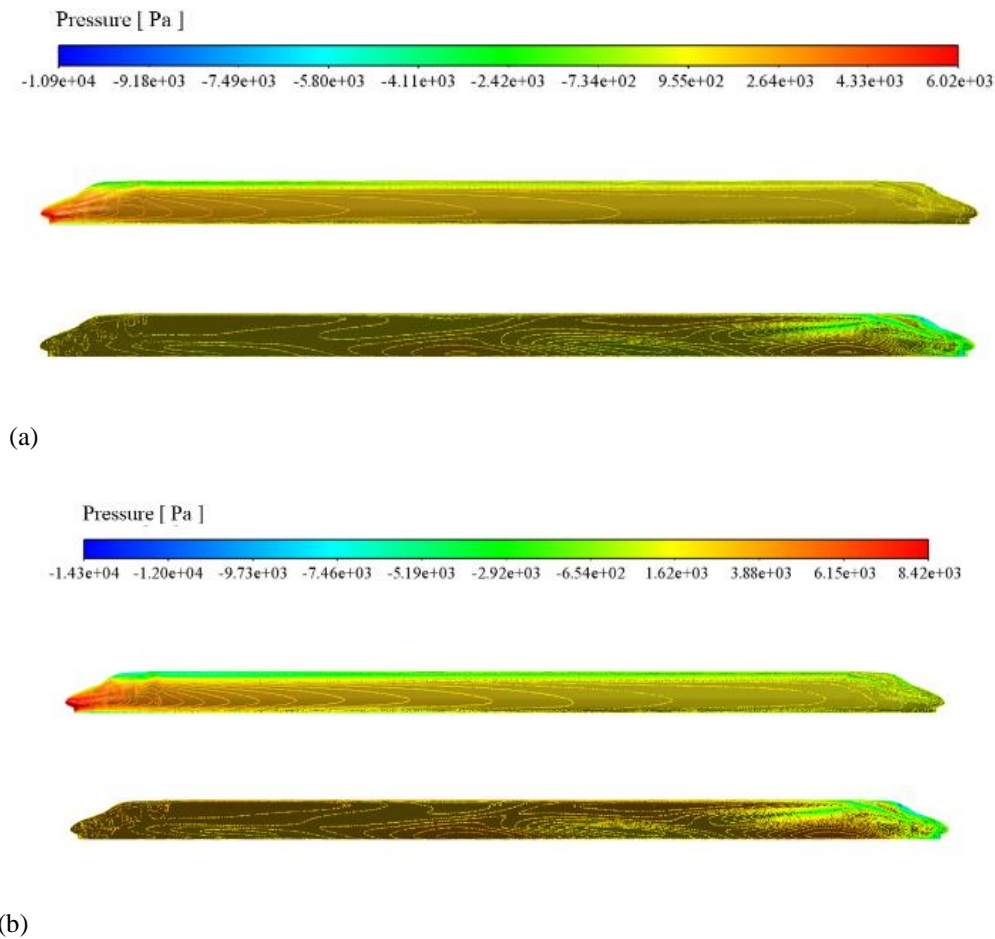
(a)

(b)

Fig. 11 Body pressure field

(a) without sand and (b) with sand

and moment caused by the increase in the wind speed. However, because the position and shape of each section of the car are not the same, the load on each section of the train is also different.

The transverse force of the three cars increased with increasing wind speed and was approximately linear with increasing wind speed, among which the transverse force of the middle car was slightly greater than that of the head car and the tail car; the resistance of the head car was significantly greater than that of the middle car and the tail car; and the resistance of the head car changed more significantly with increasing wind speed. Similarly, the change pattern of the lift force on the train body was basically the same as that of the transverse force, and the lift force on the middle car was slightly greater than that on the other two cars.

In terms of moments, the overturning moments of the three cars are significantly smaller than the nodding moments and the head shaking moments. This is because the cross-sectional areas of the trains are different in each direction. The overturning moment of the middle car is slightly larger than that of the head and tail cars, but the change in the overturning moment of the three cars with increasing wind speed is very obvious. For the nodding and shaking moments, the nodding and shaking moments

of the tail car are obviously larger than those of the head and middle cars, and the difference becomes larger with increasing wind speed.

The change in the wind–sand load on the train is related to the characteristics of the wind–sand flow itself. If the wind–sand flow cannot cross the train when it is in contact with the train, the wind–sand flow will be compressed, and the flow around the train will occur at the same time, causing an increase in the air pressure in the area. Moreover, the rapid movement of sand and wind along a train surface not only causes an increase in the surrounding pressure but also causes the train surface to exert a force parallel to the direction of movement of the sand and wind due to the viscous force generated by the sand and wind. In this paper, the wind–sand load is calculated to include the effect of the viscous force of the wind–sand flow, but since the viscous force of the wind–sand flow is small, the effect is weak compared with that of the wind–sand load, so it is not the main factor causing the change in the results. The force generated by the air pressure difference on the train is related to the surface area of each car, so the head car is subjected to a higher drag force due to frontal contact with the air flow, while the middle car is subjected to a significantly greater lateral force as well as lift force due to the larger side area; therefore, the magnitude of each moment is different.
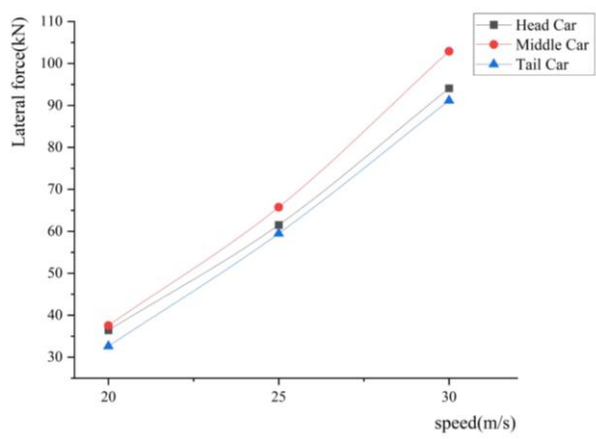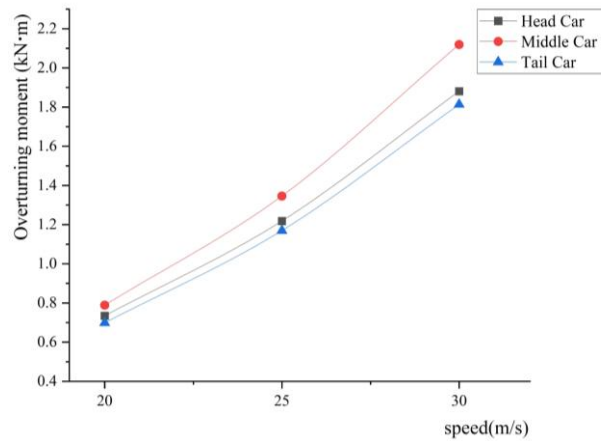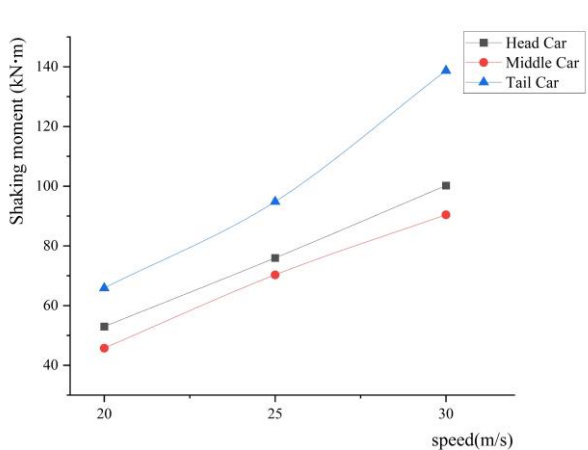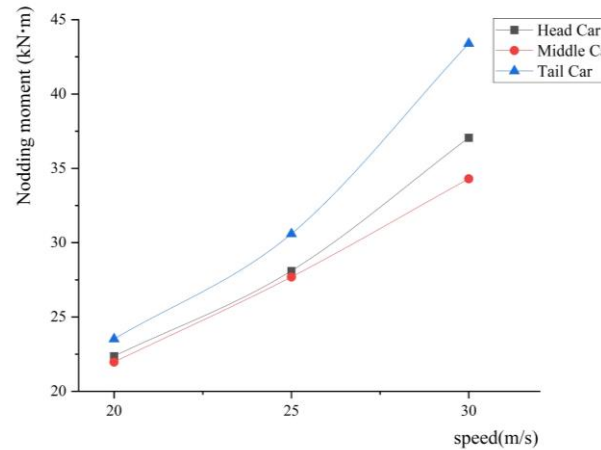
(a) Lateral force
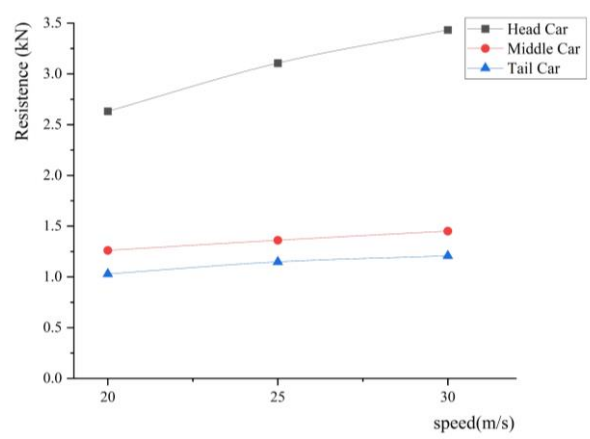
(b) Resistance
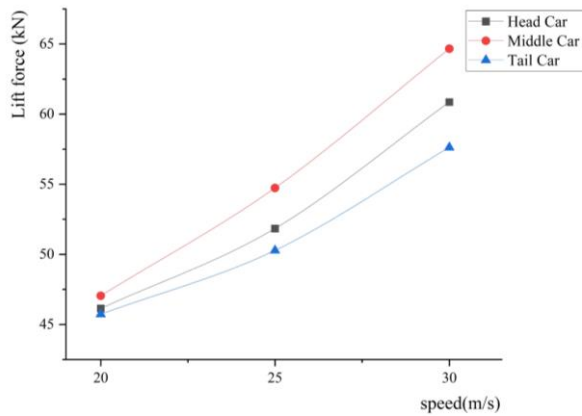
(c) Lift force

(d) Overturning moment

(e) Shaking moment

(f) Nodding moment

Fig. 12 Aerodynamic force of the train

5.   RESULT ANALYSIS

The train's running speed is proportional to the minimum curve radius. The narrower the curve radius is, the greater the driving resistance and the poorer the train operating conditions; nevertheless, a large curve radius increases the maintenance workload and expenses. According to Li (2016), the curve radius of the Lanzhou–Urumqi high-speed railway line was primarily set at 7000–10000 m, and the superelevation value of the complete line curve was determined based on an equilibrium speed of

200 km/h. The plane curve shapes are presented in Table 4, so the curve radii for the dynamic simulation computations are 7000 m, 8000 m, 9000 m, and 10000 m.

In Simpack 2021, the aerodynamic load is applied to the vehicle's center of gravity as a temporal excitation function. This load is separated into three processes, loading, continuous action, and unloading, which occur in sequence. In addition, the train travels at a speed of 250 km/h, and the wind speed is 25 m/s. The curvature radius in the model is adjusted by altering the horizontal and vertical section parameters of the line. After the simulation

Table 4 Plane Curve Statistics

Curve radius (m)	Superelevation (mm)	Number	Proportion (%)
7000	70	20	10
8000	60	48	24
9000	55	55	28
10000	50	42	21
11000	45	8	4
12000	40	24	12

Table 5 Safety indices of high-speed train operation

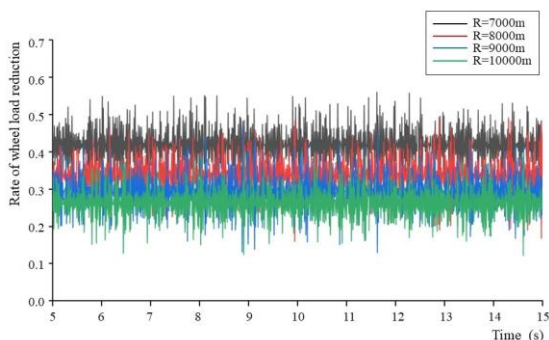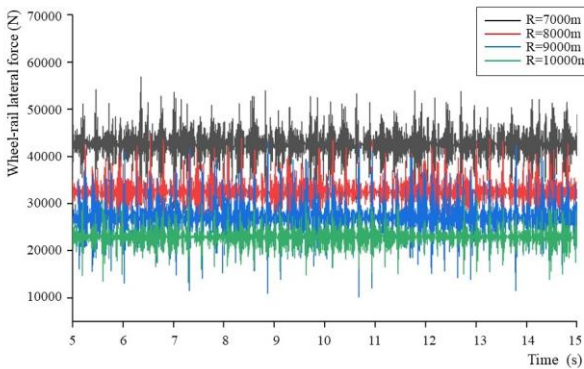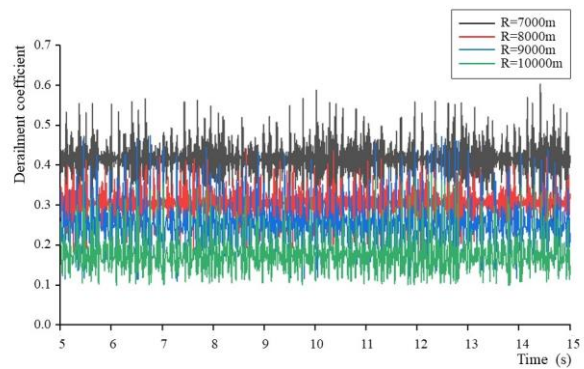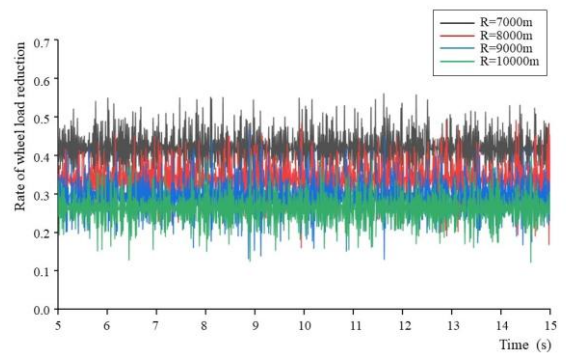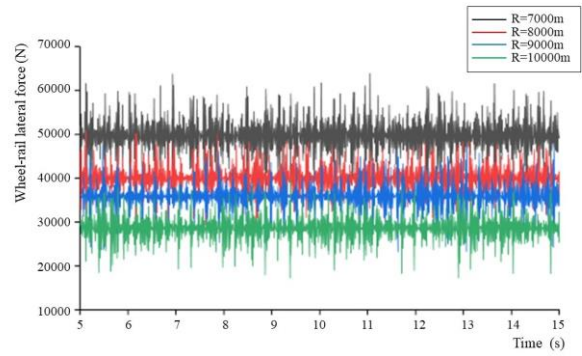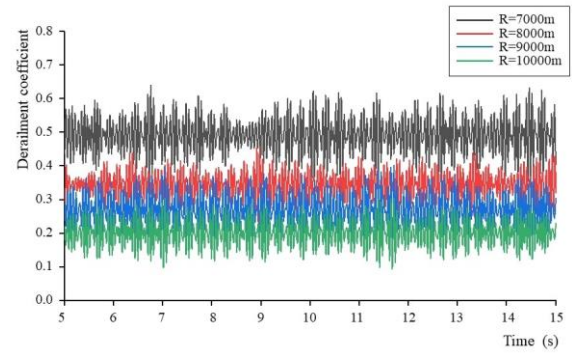| Description	Definition	Limit value
Derailment coefficient	Wheel rail lateral force/Wheel rail vertical force	≤0.8
Wheel-rail lateral force	Take 0.4 times the train's axle weight	≤68 kN
Rate of wheel load reduction	Wheel load reduction value/Average wheel load	≤0.65

Fig. 14 Safety indices of the middle car

Fig. 13 The safety indices of the head car

is completed, the values of the safety indices (Fig. 5) are obtained when the train runs on the track with different curve radii.

Figures 13–15 show the time course curves of the changes in the values of the safety indices of the three sections of the train body with increasing curve radius, and it can be seen that all of them decrease with increasing radius. Table 6 gives the maximum adverse indices of the train bodies under different curve radius conditions. When the radius was 7000 m, the maximum values of the derailment coefficients of the three car bodies were 0.603, 0.640, and 0.523; when the radius was 10000 m, the maximum values of the derailment coefficients were 0.385, 0.394, and 0.325; and the maximum value reduction rates were 36.15%, 38.44%, and 37.86%, respectively. The maximum values of the wheel–rail lateral forces of the three cars are 59.3 kN, 64.7 kN, and 57.2 kN. When the radius increased to 10000 m, the maximum wheel–rail lateral forces of the three cars were 38.2 kN, 41.1 kN, and 35.8 kN; these values were 35.58%, 36.48%, and 37.41% lower than those at a radius of 7000 m, respectively. The middle car suffered the most, followed by the head car, and the tail car suffered the least.
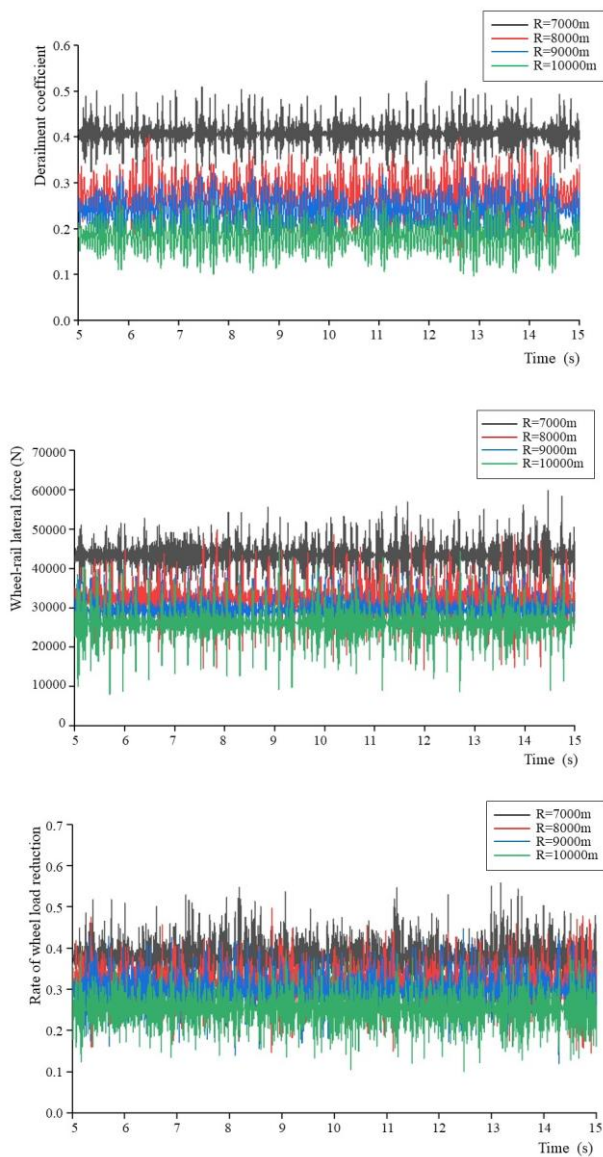
Fig. 15 The safety indices of the tail car

Table 6 The maximum adverse values of the safety indices

Derailment coefficient			
R/m	Head car	Middle car	Tail car
7000	0.603	0.64	0.523
8000	0.482	0.503	0.436
9000	0.419	0.438	0.365
10000	0.385	0.394	0.325
Wheel-rail lateral force/kN			
R/m	Head car	Middle car	Tail car
7000	59.3	64.7	57.2
8000	50.5	54.6	48.9
9000	41.2	46.1	40.6
10000	38.2	41.1	35.8
Rate of wheel load reduction			
R/m	Head car	Middle car	Tail car
7000	0.568	0.583	0.562
8000	0.489	0.507	0.472
9000	0.447	0.463	0.434
10000	0.429	0.425	0.406

Although the trend of the rate of wheel load reduction is not as obvious as the trends of the derailment coefficient and the wheel–rail lateral force, their trends are essentially the same; the wheel load reduction rate decreases with increasing radius, and the larger the radius of the curve is, the worse the effect of its reduction.

The safety index of the middle car is the most unfavorable, so only the middle car is analyzed. Figure 13 shows that the index values of the derailment coefficient, wheel–rail lateral force and wheel weight reduction rate of the medium train decrease with increasing curve radius. As the curve radius increases, the curvature gradually decreases, weakening the extrusion between the wheelset and rail. This results in a decrease in the difference between the vertical force and the transverse force of the two sides of the wheel, leading to a continuous reduction in the safety indices. When the curve radius increases from 7000 m to 9000 m, the decrease rate of each index value of the train reaches approximately 30%, but when the radius value continues to increase, the indices decrease by only approximately 7%, and the improvement effect is obviously reduced. Therefore, when operating in sandy areas, it is beneficial to increase the radius of the curve reasonably for the operation of trains.

6. CONCLUSION

In this paper, the interaction between wind–sand flow and high-speed trains is studied numerically, and the effect of changing curve radius on the running safety of trains is analyzed from the perspective of the dynamic response of vehicle–track systems. First, the flow field and aerodynamic load of the train under strong wind–sand conditions are obtained via the CFD technique. Then, a modal analysis was performed to study the dynamic response of the train to aerodynamic forces and moments and the safety of operation, and the variable considered was the wind speed. The following conclusions are drawn from the above study:

(1) By studying the effect of load on each car at different wind speeds, it is determined that the wind–sand load on the train increases with increasing wind speed, where the effect of wind speed is more significant. In addition, the lifting force, lateral force and overturning moment of the middle car are greater than those of the head and tail cars, and the drag force, nodding moment and rocking moment are lower; the opposite is true for the head and tail cars.

(2) The dynamic performance of the vehicle body for a head–middle–tail train is basically the same under different wind–sand loads, in which the wind and sand effects on the middle car have the greatest impact and the most unfavorable safety indices; thus, the middle car is most likely to derail or overturn;

(3) Finally, by changing the curve radius, it is found that increasing the radius can reduce the wheel–rail lateral force, the derailment coefficient and the wheel weight reduction rate of the train, thus improving train safety; however, when the radius increases to a certain value, the improvement effect is not obvious.

Therefore, when designing the curved section of a high-speed railway in a sandstorm area, it is recommended that the curve radius be increased as much as possible. However, selecting a curve radius that is too large may weaken the effect of improving operating safety, and it will also increase the difficulty of laying, maintaining, and repairing the line. When the radius reaches a certain threshold, the positive vector value becomes very small, making it difficult to ensure the accuracy of the minimal positive vector value and potentially causing track irregularities. Therefore, it is recommended to measure 8000-9000 m. This study presents an analysis of the influence of the curve radius on the dynamic performance of trains and provides some references for mitigating disasters at sandy railways and determining other similar high-speed railway line designs. When selecting the curve radius in the wind-blown sand area for a high-speed railway project, it is important to consider local wind and sand data as well as design standards. The value of the mitigation curve and the superelevation should also be accounted for. Additionally, building a windbreak wall can help reduce harm. Notably, other parameters, such as gentle curves and vertical curves, are also worth studying.

ACKNOWLEDGEMENTS

CONFLICT OF INTEREST

The authors declare that they have no known competing financial interests or personal relationships that could have appeared to influence the work reported in this paper.

AUTHORS CONTRIBUTION

Y Bai: Conceived and performed the finite element analysis and interpreted the results; **Z. N. Zhang:** Examined the results, corrected the paper and edited the manuscript; **Z. F. Wang:** Assisted in data collection; **T. M. Li:** Reviewed the manuscript; **Y. J. Wang:** Provided guidance.

REFERENCES

Adamu, A., Zhang, J., Gidado, F., & Wang, F. (2022). An investigation of influence of windshield configuration and train length on high-speed train aerodynamic performance. *Journal of Applied Fluid Mechanics, 16*(2), 337-352. https://doi.org/10.47176/JAFM.16.02.1433

Andersson, E., Nilstam, N. G., & Ohlsson, L. (1996). Lateral track forces at high speed curving comparisons of practical and theoretical results of Swedish high speed train x2000. *Vehicle System Dynamics, 25*(S1), 37-52. https://doi.org/10.1080/00423119608969186

Baker, C., Cheli, F., Orellano, A., Paradot, N., Proppe, C., & Rocchi, D. (2009). Cross-wind effects on road and rail vehicles. *Vehicle System Dynamics, 47*(8), 983-1022. https://doi.org/10.1080/00423110903078794

Bergstrom, D. J., Boucher, K. M., & Derksen, D. (1992). Wind flow over an elevated roadway. *Journal of Wind Engineering and Industrial Aerodynamics, 44*(1-3), 2697-2698. https://doi.org/10.1016/B978-0-444-81688-7.50017-6

Bruno, L., Horvat, M., & Raffaele, L. (2018). Windblown sand along railway infrastructures: A review of challenges and mitigation measures. *Journal of Wind Engineering and Industrial Aerodynamics, 177*, 340-365. https://doi.org/10.1016/j.jweia.2018.04.021

Chang, C., Li, T., Qin, D., & Zhang, J. (2021). On the scale size of the aerodynamic characteristics of a high-speed train. *Journal of Applied Fluid Mechanics, 15*(1), 209-219. https://doi.org/10.47176/JAFM.15.01.33041

Cheng, J. J., & Xue, C. X. (2014). The sand-damage–prevention engineering system for the railway in the desert region of the Qinghai-Tibet plateau. *Journal of Wind Engineering and Industrial Aerodynamics, 125*, 30-37. https://doi.org/10.1016/j.jweia.2013.11.016

Deng, E., Yang, W., He, X., Zhu, Z., Wang, H., Wang, Y., ... & Zhou, L. (2021a). Aerodynamic response of high-speed trains under crosswind in a bridge-tunnel section with or without a wind barrier. *Journal of Wind Engineering and Industrial Aerodynamics, 210*, 104502. https://doi.org/10.1016/j.jweia.2020.104502

Deng, G., Ma, W., Peng, Y., Wang, S., Yao, S., & Peng, S. (2021b). Experimental study on laminated glass responses of high-speed trains subject to windblown sand particles loading. *Construction and Building Materials, 300*, 124332. https://doi.org/10.1016/j.conbuildmat.2021.124332

Du, J., Yang, M., Zhang, L., Wu, F., & Huang, W. (2020). Numerical simulation of aerodynamics of train with broken windows. *Journal of Applied Fluid Mechanics, 13*(5), 1443-1452. https://doi.org/10.36884/jafm.13.05.30951

Feng, L. C., & Lu, J. Q. (1994). Summary of railway sand damage control in sandy areas of China. *Journal of Desert Research, 14*(3), 7. http://www.desert.ac.cn/CN/Y1994/V14/I2/47

Gao, Y., Zhang, W. M., Tan, L. H. (2018). Geomorphologic mapping of wind-blown sand and causes of wind-blown sand disaster in Tieyandun gale area of Lanxin high-speed. *Journal of Desert Research, 38*(03), 500-507. https://doi.org/10.7522/j.issn.1000-694X.2017.00070

Hemida, H., Krajnovic, S., & Davidson, L. (2005, June). *Large-eddy simulation of the flow around a simplified high speed train under the influence of a cross-wind.* 17th AIAA Computational Fluid Dynamics Conference (p. 5354). https://www.tfd.chalmers.se/~lada/postscript_files/hassan_2005_5354.pdf

Jiang, F. Q., Li, Y., Li, K. C. (2010). Study on structural

characteristics of wind-blown sand flow in Baili wind area of Lanzhou-Xin Railway. *Journal of Railway Science, 32*(3), 6. http://doi.org/10.3969/j.issn.1001-8360.2010.03.019

Jiang, P., Pan, X. M., Xue, J. M., & Sha, Y. P. (2020). Comparative analysis of wind characteristics in the strongest wind area along Xinjiang railway. *Journal of Meteorology and Environment, 36*(5), 7. https://doi.org/10.3969/j.issn.1673-503X.2020.05.009

Khier, W., Breuer, M., & Durst, F. (2000). Flow structure around trains under side wind conditions: a numerical study. *Computers & Fluids, 29*(2), 179-195. https://doi.org/10.1016/S0045-7930(99)00008-0

Krajnović, S., Ringqvist, P., Nakade, K., & Basara, B. (2012). Large eddy simulation of the flow around a simplified train moving through a crosswind flow. *Journal of Wind Engineering and Industrial Aerodynamics, 110*, 86-99. https://doi.org/10.1016/j.jweia.2012.07.001

Li, K., Jiang, F., Xue, C., Yang, Y. & Ge, S. (2010). Analysis on the characteristics of Gobi wind sand flow in Xijianfang section of Lanzhou-Xin Railway. *Journal of Railway Engineering*, (3), 4. https://doi.org/10.3969/j.issn.1006-2106.2010.03.004

Li, R. (2016). Study on adaptability of passenger trains with constant speed running on Lanzhou-New Passenger dedicated line. *Railway Transportation and Economy, 38*(5), 5. https://doi.org/10.16668/j.cnki.issn.1003-1421.2016.05.06

Li, T. (2012). *Research on fluid-structure coupling calculation method and dynamic performance of high-speed train* [Ph.D. thesis, Southwest Jiaotong University]. https://kns.cnki.net/KCMS/detail/detail.aspx?dbname=CDFD1214&filename =1013106871.nh

Li, T., Zhang, J. Y., & Zhang, W. H. (2012a). Joint simulation of fluid-structure coupling dynamics of high-speed train under cross wind. *Journal of Vibration Engineering, 25*(2), 8. https://doi.org/10.3969/j.issn.1004-4523.2012.02.006

Li, T., Zhang, J. Y., & Zhang, W. H. (2012b). Safety analysis of high-speed train operation under sandstorm environment. *Sichuan Mechanics Society annual conference.* http://106.37.81.211:8082/images/sjsimages/pdf/hy/h074421/pdf/H074421002.pdf

Li, T., Zhang, J. Y., Li, Z. J., & Zhang, W. H. (2012c). Co-simulation on fluid-structure interaction of high-speed train based on Fluent and Simpack. *Chinese Journal of Computational Mechanics, 29*(5), 675-680. http://www.cqvip.com/qk/94820a/201205/43665665.html

Liu, D., Wang, Q., Zhong, M., Lu, Z., Wang, J., Wang, T.,

& Lv, S. (2019). Effect of wind speed variation on the dynamics of a high-speed train. *Vehicle System Dynamics, 57*(2), 247-268. https://doi.org/10.1080/00423114.2018.1459749

Liu, D., Wang, T., Liang, X., Meng, S., Zhong, M., & Lu, Z. (2020). High-speed train overturning safety under varying wind speed conditions. *Journal of Wind Engineering and Industrial Aerodynamics, 198*, 104111. https://doi.org/10.1016/j.jweia.2020.104111

Liu, J., Yu, M., Zhang, J. & Zhang, W. (2011). Research on safety of high-speed train running in cross wind based on large eddy simulation. *Journal of Railway Science, 33*(4), 13-21. https://doi.org/10.3969/j.issn.1001-8360.2011.04.003

Meng, X. L., Li, K., Xie, S. B. (2018). Strong wind environmental characteristics and countermeasures according to engineering divisions along a high-speed railway. *Journal of Desert Research, 38*(5), 972-977. https://doi.org/10.7522/j.issn.1000-694X.2017.00063

Montenegro, P. A., Ribeiro, D., Ortega, M., Millanes, F., Goicolea, J. M., Zhai, W., & Calçada, R. (2022). Impact of the train-track-bridge system characteristics in the runnability of high-speed trains against crosswinds-Part II: Riding comfort. *Journal of Wind Engineering and Industrial Aerodynamics, 224*, 104987. https://doi.org/10.1016/j.jweia.2022.104987

Niu, B., Tan, L., Zhang, X. J., Qu, J., An, Z., Wang, J., & Li, K. (2020). Targeted control of sand hazards for a railway in extremely arid regions using fingerprinting approaches. *Geomorphology, 361*, 107189. https://doi.org/10.1016/j.geomorph.2020.107189

Noguchi, Y., Suzuki, M., Baker, C., & Nakade, K. (2019). Numerical and experimental study on the aerodynamic force coefficients of railway vehicles on an embankment in crosswind. *Journal of Wind Engineering and Industrial Aerodynamics, 184*, 90-105. https://doi.org/10.1016/j.jweia.2018.11.019

Paz, C., Suárez, E., Gil, C., & Concheiro, M. (2015). Numerical study of the impact of windblown sand particles on a high-speed train. *Journal of Wind Engineering and Industrial Aerodynamics, 145*, 87-93. https://doi.org/10.1016/j.jweia.2015.06.008

Sharratt, B. S., & Vaddella, V. (2014). Threshold friction velocity of crusted windblown soils in the Columbia Plateau. *Aeolian Research, 15*, 227-234. https://doi.org/10.1016/j.aeolia.2014.08.002

Srivastava, S., Sivasankar, G., & Dua, G. (2022). A review of research into aerodynamic concepts for high speed trains in tunnels and open air and the air-tightness requirements for passenger comfort. *Proceedings of the Institution of Mechanical Engineers, Part F: Journal of Rail and Rapid Transit, 236*(9), 1011-1025. https://doi.org/10.1177/09544097211072973

Sun, S. F., & Zhang, G. X. (2019). Characteristics of near-formation vertical wind shear index in the Baili wind region of Xinjiang. *Journal of Desert and Oasis*

Meteorology, 13(3), 6. https://doi.org/10.12057/j.issn.1002-0799.2019.03.014

Suzuki, M., Tanemoto, K., & Maeda, T. (2003). Aerodynamic characteristics of train/vehicles under cross winds. *Journal of Wind Engineering and Industrial Aerodynamics, 91*(1-2), 209-218. https://doi.org/10.1016/S0167-6105(02)00346-X

Wang, J., Liu, D., Gao, G., Zhang, Y., & Zhang, J. (2019). Numerical investigation of the effects of sand collision on the aerodynamic behaviour of a high-speed train subjected to yaw angles. *Journal of Applied Fluid Mechanics, 12*(2), 379-389. https://doi.org/10.29252/jafm.12.02.28788

Wang, M., Li, X. Z., Xiao, J., Zou, Q. Y., & Sha, H. Q. (2018). An experimental analysis of the aerodynamic characteristics of a high-speed train on a bridge under crosswinds. *Journal of Wind Engineering and Industrial Aerodynamics, 177*, 92-100. https://doi.org/10.1016/j.jweia.2018.03.021

Woldman, M., van der Heide, E., Schipper, D. J., Tinga, T., & Masen, M. A. (2012). Investigating the influence of sand particle properties on abrasive wear behaviour. *Wear, 294*, 419-426. https://doi.org/10.1016/j.wear.2012.07.017

Wu, J. J, Sun, H. Q., & He, L. H. (2010). Study on influencing factors of starting wind speed of sand grains. *Journal of Desert Research, 30*(4), 743-748. http://www.desert.ac.cn/CN/Y2010/V30/I4/743

Wu, Z., & Cao, Y. (2015). Numerical simulation of flow over an airfoil in heavy rain via a two-way coupled Eulerian–Lagrangian approach. *International Journal of Multiphase Flow, 69*, 81-92. https://doi.org/10.1016/j.ijmultiphaseflow.2014.11.006

Xi, Y. (2012). *Research on aerodynamic characteristics and operating safety of high-speed trains under cross wind* [PhD thesis, Beijing Jiaotong University]. https://kns.cnki.net/KCMS/detail/detail.aspx?dbname= CDFD1214&filename=1012318704.nh

Xiao, J. H., Yao, Z. Y., Qu, J. J., & Jiang, F. F. (2016). Characteristics and formation mechanism of extreme wind conditions in Baili wind area of Lanzhou-Xin Railway. *Chinese Railway Science, 37*(3), 130-137. https://doi.org/10.3969/j.issn.1001-4632.2016.03.19

Xiong, H. B., Yu, W. G., Chen, D. W., & Shao, X. M. (2011). Numerical study on the aerodynamic performance and safe running of high-speed trains in sandstorms. *Journal of Zhejiang University-SCIENCE A, 12*(12), 971-978. https://doi.org/10.1631/jzus.A11GT005

You, W., Kwon, H., Park, J., & Shin, Y. (2018). Effect of wind gusts on the dynamics of railway vehicles running on a curved track. *Proceedings of the Institution of Mechanical Engineers, Part F: Journal of Rail and Rapid Transit, 232*(4), 1103-1120. https://doi.org/10.1177/0954409717708924

Yu, M., Liu, J., Li, T. & Zhang, Q. (2021). Safety characteristics of high-speed train operation under strong wind and rain environment. *Chinese Journal of Mechanical Engineering, 57*(20), 172-180. https://doi.org/10.3901/JME.2021.20.172

Zhang, J., Gao, G. J., Liu, T. H., & Li, Z. W. (2015). Crosswind stability of high-speed trains in special cuts. *Journal of Central South University, 22*(7), 2849-2856. https://doi.org/10.1007/s11771-015-2817-y

Zhang, J., Gao, G., Liu, T., & Li, Z. (2017a). Shape optimization of a kind of earth embankment type windbreak wall along the Lanzhou-Xinjiang railway. *Journal of Applied Fluid Mechanics, 10*(4), 1189-1200. https://doi.org/10.18869/ACADPUB.JAFM.73.241.27353

Zhang, J., He, K., Wang, J., Liu, T., Liang, X., & Gao, G. (2019a). Numerical simulation of flow around a high-speed train subjected to different windbreak walls and yaw angles. *Journal of Applied Fluid Mechanics, 12*(4), 1137-1149. https://doi.org/10.29252/JAFM.12.04.29484

Zhang, J., He, K., Xiong, X., Wang, J., & Gao, G. (2017b). Numerical simulation with a DES approach for a high-speed train subjected to the crosswind. *Journal of Applied Fluid Mechanics, 10*(5), 1329-1342. https://doi.org/10.18869/ACADPUB.JAFM.73.242.27566

Zhang, K. C., Qu, J. J., Yu, Y. P. (2019b). Research progress of railway wind-blown sand control in China. *Advances in Earth Science,* (06), 573-583. https://doi.org/10.11867/j.issn.1001-8166.2019.06.0573

Zhang, Z., Pan, K., Zhang, Y., & Han, L. (2023). Sand transport characteristics above gobi surface during a dust storm in northern china. *Journal of Desert Research, 43*(2), 130-138. http://doi.org/10.7522/j.issn.1000-694X.2022.00096